Structural Evolution of Nanograins during Cold Crystallization of Poly(9,9-di-*n*-octyl-2,7-fluorene) As Revealed via in Situ Small-Angle X-ray Scattering/Wide-Angle X-ray Scattering/Differential Scanning Calorimetry

C. H. Su,[†] U. Jeng,*[,†] S. H. Chen,[‡] S. J. Lin,[‡] Y. T. Ou,[‡] W.-T. Chuang,[†] and A. C. Su*[,§]

National Synchrotron Radiation Research Center, Science-Based Industrial Park, Hsinchu 300, Department of Materials Science and Engineering, National Dong Hwa University, Hualien 974, and Department of Chemical Engineering, National Tsing Hua University, Hsinchu 300, Taiwan

Received May 27, 2008; Revised Manuscript Received August 19, 2008

ABSTRACT: By means of in situ small-angle X-ray scattering/wide-angle X-ray scattering/differential scanning calorimetry (SAXS/WAXS/DSC), structural evolution of poly(9,9-di-*n*-octyl-2,7-fluorene) (PFO) in a cold crystallization process was quantitatively examined. After removal of background scattering from the fractal-like structure, SAXS profiles obtained during programmed heating of an amorphous PFO specimen unveil a sequence of stages of structural evolution. These include (1) a frozen-in stage below the glass transition temperature ($T_g \approx$ 62 °C), (2) the nucleation of prolate nanograins with radius of gyration $R_g \approx 3.3$ nm from 65 to 85 °C, (3) growth of the prolate ellipsoids up to $R_g \approx 5.0$ nm between 95 and 105 °C, and (4) coalescence (and thickening) of the nanocrsytals into oblates (of $R_g \approx 10$ nm) upon further heating to 145 °C. There were no further changes in morphological features in the subsequent isothermal annealing at 145 °C for up to 1 h, as the size of the coalesced nanograins quickly reached a threshold value where the orientation and attachment of neighboring nanograins via thermally activated Brownian rotation became seriously hindered. Developments in the DSC-determined crystallinity ($X_{c,DSC}$) and the degree of heterogeneity (Q_{inv} from SAXS) coincided with the nucleation and growth stages, respectively; in contrast, buildup of the WAXS-determined crystallinity ($X_{c,WAXS}$) proceeded mainly in the subsequent coalescence stage where large nanocrystallites were developed.

Introduction

We previously reported that solution-cast films of conjugated polymers with grafted alkyl side chains comprise clearly identifiable domains ca. 10 nm in size upon solvent evaporation.[1−7] The origin of the nanodomains is not clear but was postulated to be the collapse of intrinsically amphiphilic (aromatic vs aliphatic) chains during solvent removal. In the case of crystalline poly(9,9-di-*n*-octyl-2,7-fluorene) (PFO) and its homologues, these nanodomains appear to serve as basic units for morphological development upon melt crystallization.[5−7] We have subsequently examined the morphology of PFO cold-crystallized at the same temperature range of the preceding melt crystallization studies to better understand the effects of the nanodomain morphology on the crystallization behavior.[8] On the basis of mainly scanning (SEM) and transmission (TEM) electron microscopy observations, with supporting evidence from *parallel* experiments of differential scanning calorimetry (DSC), grazing-incidence wide-angle X-ray scattering (GI-WAXS), and small-angle X-ray scattering (SAXS), we concluded *qualitatively* that cold crystallization of PFO involves intradomain nucleation, followed by nanodomain alignment and coalescence into fibrils on the submicrometer length scale via thermally activated Brownian adjustment of the nanodomain orientation.[8] An analogy with "oriented aggregation"[9] or "oriented attachment and coalescence"[10] behavior of inorganic nanocrystals was therefore drawn. Details of the structural evolution of PFO nanograins, however, were difficult to trace with the *after-the-fact* approach in our previous microscopic studies.

Here we report a *quantitative* analysis of in situ SAXS/WAXS/DSC results (obtained simultaneously over a single sample using synchrotron radiation) to elucidate the structural evolution of PFO nanograins in chronological increments. Integrated structural information obtained from the combined tools indicates that cold crystallization of PFO involves a sequence of events which may be categorized as nucleation, growth, and coalescence of nanograins. Relevance to issues of precrystallization ordering and density fluctuations prior to crystallization of general polymers, specifically the spinodal mechanism[11] in cold crystallization and the mesophase hypothesis[12] in melt crystallization, is discussed.

Experimental Details

The PFO sample was purchased from American Dye Source, Quebec, Canada (catalog no. ADS129BE). The weight-averaged molecular mass (M_w) was 65 kDa, with a polydispersity index (PDI) of 2.6 as determined via gel permeation chromatography using polystyrene standards. In situ SAXS/WAXS/DSC measurements were performed at beamline 17B3 of the National Synchrotron Radiation Research Center (NSRRC).[13] The glassy PFO specimen (ca. 0.5 mm in thickness and 7 mm in diameter, liquid nitrogen quenched from the nematic phase at 200 °C, i.e., significantly above the equilibrium melting temperature of 179 °C)[14] was placed between two Kapton films and encapsulated in an aluminum cell where both the cap and the pan were punctured to give X-ray windows ca. 4 mm in diameter. The sample cell was then placed in the Mettler Toledo FP84 DSC cell holder modified slightly for simultaneous SAXS/WAXS/DSC measurements. Specifically, the aluminum sample cell placed inside the DSC instrument was fixed by a silicon O-ring when the DSC instrument was positioned vertically (edge-up) to accept the horizontally incident X-ray beam (0.5 mm in diameter) through the entrance hole (2 mm in diameter); the exit window of the DSC instrument was enlarged to 7 mm in

---

[†] National Synchrotron Radiation Research Center.
[‡] National Dong Hwa University.
[§] National Tsing Hua University.

10.1021/ma801177h CCC: $40.75 © 2008 American Chemical Society
Published on Web 10/04/2008

diameter for a better WAXS range. Comparable melting traces were obtained for test samples using modified or intact DSC cells. The modification of DSC for X-ray scattering, first done by Bark and Zachmann 15 years ago,[15] has been comprehensively reviewed by Chu and Hsiao.[16]

With the 8 keV (wavelength $\lambda = 1.55$ Å) beam, SAXS, WAXS, and DSC data were simultaneously collected using respectively 2-D and 1-D linear proportional counters and the DSC instrument during heating (at 10 °C/min) of the specimen from 30 to 145 °C and subsequent annealing at 145 °C for 1 h. With an available photon flux of ca. 10^9 photons/s, the SAXS/WAXS data collection time was set to 1 frame/min throughout the entire heating/annealing process. Limited by the geometry of the SAXS/WAXS/DSC setup, we compromised the WAXS detecting q region to 0.8−1.5 $Å^{-1}$ for a wider SAXS q region of 0.006−0.25 $Å^{-1}$; the corresponding sample-to-detector distances for the SAXS and WAXS detectors were 2700 and 750 mm, respectively. Here, the scattering wave vector, defined as $q = 4\pi\lambda^{-1} \sin \theta$ (with 2θ the scattering angle), was calibrated using silver behenate, sodalite, and silicon powders filled in a cell with a 1 mm X-ray path length under the same PFO sample environment. A high-density polyethylene standard (1.90 mm in thickness) with a known absolute peak intensity of 36.6 cm^{-1} at $q = 0.0227$ $Å^{-1}$ was used to obtain the scaling constant between the measured $I(q)$ and the absolute intensity; the scaling constant was then applied to PFO sample measurements for the absolute intensity scale. Scattering data were further corrected for sample transmission, background, and detector sensitivity.[13] Experimental reproducibility was generally confirmed by repeated runs using fresh specimens.

To obtain the changes in the (110) and (200) reflections, parallel WAXS with a broader q range (0.2−2.1 $Å^{-1}$) was furthermore performed at the powder X-ray diffraction end station of the NSRRC 01C beamline (16 keV, $\lambda = 0.775$ Å, and sample-to-detector distance 324.3 mm). All other experimental parameters were kept unaltered; i.e., the same specimen preparation procedure, the same DSC setup, and the same heating rate, etc., were adopted.

Data Analysis

With $P(q)$ the normalized form factor (i.e., $P(0) = 1$), $S(q)$ the structure factor, and $I_o = n_p(\Delta\rho)^2V^2$, the zero-angle scattering intensity depending on the nanograin concentration n_p, nanograin volume V, and scattering contrast $\Delta\rho$, SAXS profiles were modeled according to[17,18] $I(q) = I_oP(q)\ S(q)$, which is often used in the SAXS analysis for a colloidal solution. We assumed constant scattering contrast between the nanograins and the matrix: density changes due to thermal expansion in the amorphous phase and solidification of nanograins were neglected.

For an ellipsoid with semimajor axis A and semiminor axis B, the form factor averaged for spatial orientation is given by $P(q) = \int_0^1 |3j_1(v)/v|^2\, d\mu$, where $v = q[A^2\mu^2 + B^2(1 - \mu^2)]^{1/2}$ and j_1 is the spherical Bessel function of the first order.[17,18] The scattering invariant Q_{inv} commonly used to quantify the level of heterogeneity in two-phase systems[18−21] is expressed as $Q_{inv} = \int_0^\infty I(q)q^2\, dq$ (with units of $Å^{-4}$ in our case). For convenience in comparison, a relative scattering invariant can be calculated with the upper and lower limits of the integration replaced by the high-q and low-q limits of the SAXS profiles.[18] Such an approximation is appropriate when the experimental q range covers major changes of the SAXS profiles.

The *relative* crystallinity $X_{c,WAXS}$, obtained from the WAXS profile based on the integrated intensity over the observed crystalline reflections, is normalized with respect to the *maximum* crystallinity observed. Likewise, the relative crystallinity $X_{c,DSC}$, obtained from a DSC trace based on the integrated heat flow up to a temperature T, is normalized to the *total* heat flow integrated over the entire DSC trace.

Results

Nematic Background. The nematic phase of the PFO was evidenced from polarized light microscopy (PLM) and discussed in our previous studies.[6,7] Figure 1 illustrates coinciding SAXS profiles of the PFO specimen measured either at 168 °C as a nematic melt or at room temperature as a quenched (from 200 °C using liquid nitrogen) nematic glass. The result indicates that nanostructural features of the nematic phase of PFO are well preserved during quenching, and the SAXS intensity contributed by the PFO nematic phase follows the power-law behavior of $I(q) \approx q^p$ with $p = -3.4 \pm 0.1$ for $q \leq 0.03$ $Å^{-1}$.

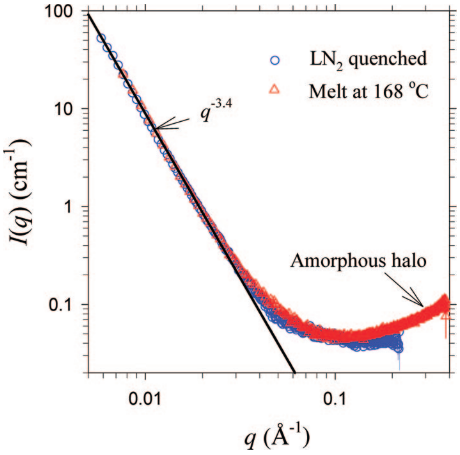

Figure 1. Respective SAXS profiles obtained at 168 °C and at room temperature after liquid nitrogen quenching from 200 °C. The solid line indicates the fitted power law $I(q) \approx q^{-3.4}$.

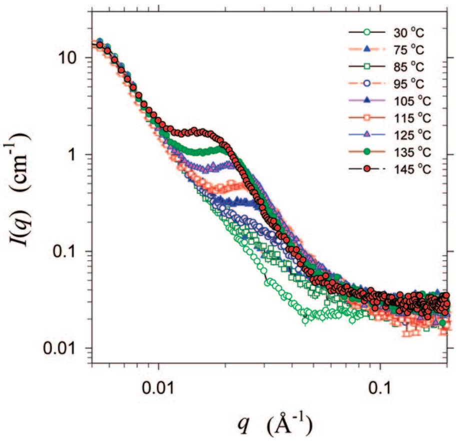

Figure 2. Temperature-dependent SAXS profiles obtained during heating from 30 to 145 °C. For clarity, not all data are shown.

In the surface fractal model,[22] scattering dominated by a fractal surface morphology is described by $I(q) \approx q^{-(6-D_s)}$ with the surface fractal dimension D_s between 2 and 3 (with 2 for ideally flat surfaces), leading to possible p values between −4 and −3. The present case of $p = -3.4$ corresponds to $D_s = 2.6$, signifying fairly rough nanodomain surfaces. The term "surface" used here corresponds to the *interface* between the more densely packed interior of nanodomains and the loosely packed interdomain region. Similar fractal surfaces have been observed[4] for nanodomains in solution-cast films of noncrystalline poly(2-methoxy-5-(2′-ethylhexyloxy)-1,4-phenylenevinylene) (MEH-PPV).

Nanostructural Development. Shown in Figure 2 are temperature-dependent SAXS profiles of the PFO specimen from room temperature (ca. 30 °C) to 145 °C. As the temperature was raised above the T_g (62 °C) of PFO,[6] additional scattering (other than that contributed by the nematic phase) emerged in the higher q region (0.02−0.2 $Å^{-1}$). This additional scattering developed with increasing temperature up to 145 °C but changed little in the subsequent 1 h isothermal annealing at 145 °C, indicating that the kinetic process involved is quickly

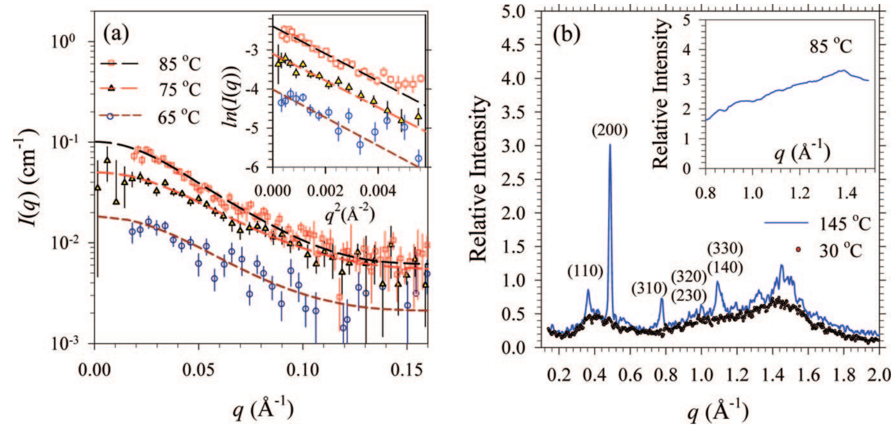

Figure 3. (a) Reduced SAXS profiles obtained at 65, 75, and 85 °C, each fitted with a model of monodisperse ellipsoids (dashed curves). The inset shows corresponding Guinier plots with $R_g \approx 3.3$ nm. (b) WAXS profiles obtained from an in-house X-ray diffractometer with a PFO sample (of the same thermal history) at 30 °C and 10 min after reaching 145 °C. The inset shows the WAXS halo obtained simultaneously with the SAXS profile at 85 °C.

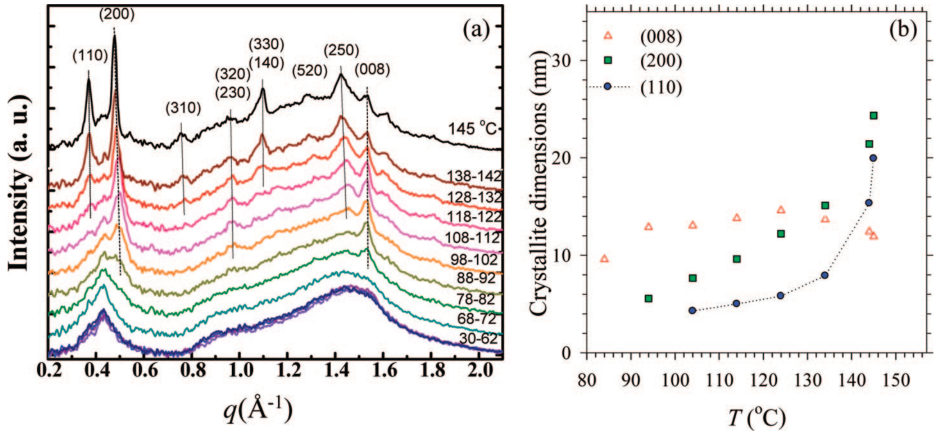

Figure 4. (a) Full WAXS profiles obtained during heating (10 °C/min) from 30 to 145 °C in a parallel experiment performed at the powder X-ray diffraction end station of the 01C beamline, NSRRC. From the background of the broad “nematic streak” (from 0.3 to 0.6 $Å^{-1}$) and amorphous ring (0.8 to 2.0 $Å^{-1}$), there emerged first the (008) reflection at ca. 80 °C, followed by the (200) reflection beyond 90 °C, and then the (*hk*0) reflections upon further increases in temperature above 100 °C. This implies a sequence of molecular ordering: first stretching along the backbone, followed by improved transverse packing along the crystallographic *b* axis, and then further ordering along the crystallographic *a* axis. (b) Corresponding temperature-dependent crystallite dimensions extracted from the reflection peak widths using the Scherrer equation.

completed on the time scale of 1 min or so. All SAXS profiles shown in Figure 2 contain a common contribution from the nematic phase (cf. the power-law scattering in Figure 1). Removal of this constant scattering of the nematic phase from the as-obtained SAXS profiles gives the scattering contribution directly related to the structural evolution of PFO nanograins. As detailed below, the reduced SAXS profiles clearly reveal features of nucleation, growth, and coalescence of nanograins.

Nucleation. Illustrated in Figure 3a are SAXS profiles measured at 65, 75, and 85 °C, with the contribution from the nematic phase subtracted. On the basis of the Guinier approximation[17,18] (dashed lines, inset of Figure 3a), a common value $R_g \approx 3.3 \pm 0.2$ nm for the radius of gyration of nanograins can be extracted from the three sets of data. To determine the shape of the nanograins, we fitted the SAXS profiles with possible form factors of spheres, disks, rods, and ellipsoids; it turned out that the profiles were best fitted with ellipsoids. Shown in Figure 3a are correspondingly fitted profiles using semimajor axis $A = 6.4 \pm 0.9$ nm and semiminor axis $B = 2.4 \pm 0.7$ nm but different I_o values of 0.018, 0.045, and 0.095 cm^{-1}, respectively, for the three sets of data measured at 65, 75, and 85 °C. The corresponding radius of gyration, as calculated from[18] $R_g = [(A^2 + 2B^2)/5)]^{1/2}$, is 3.3 ± 0.3 nm, in agreement with that obtained from the model-independent Guinier approximation.

The fairly well represented SAXS profiles by model fitting indicate the formation of nanograins above T_g (≈ 62 °C), followed by a nearly 5-fold increase in the number density n_p (as estimated from I_o) from 65 to 85 °C, with the size and shape of nuclei remaining unchanged. Due to the lack of long-range positional order in nuclei of such a limited size, the nucleation of PFO resulted in no discernible peaks in the concomitant WAXS profile at 85 °C (inset of Figure 3b), which is essentially unchanged within this temperature range of mainly nucleation stage. However, the density within the nucleus must be rather close to the crystal density to give adequate contrast for the clearly observable changes in the SAXS profiles. For comparison, the full WAXS profile (Figure 3b, obtained using an in-house X-ray diffractometer for a PFO specimen cold-crystallized at 145 °C for 10 min) exhibits clear reflections in a wide *q* range, including the region (0.8−1.5 $Å^{-1}$) monitored by the simultaneous WAXS.

To reaffirm this lack of long-range positional order within the nuclei, in situ WAXS covering an extended *q* range (0.2−2.1 $Å^{-1}$) was performed (cf. the last paragraph in the Experimental Details). The full WAXS profiles (Figure 4a) indeed support the notion of a frozen-in state below T_g and the general absence of 3-D long-range positional order during the nucleation stage of 65−85 °C. More importantly, these in situ WAXS profiles suggest sequential molecular ordering, as illustrated by the

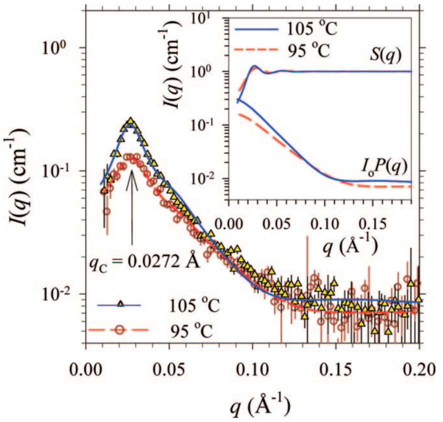

Figure 5. SAXS profiles obtained at 95 and 105 °C, each fitted with a combination of ellipsoid form factor $P(q)$ and hard-sphere structure factor $S(q)$. The inset shows the corresponding $I_oP(q)$ and $S(q)$ profiles extracted from the model fitting.

evolutions of the crystallite dimensions extracted from the reflection peak widths using the Scherrer equation (Figure 4b). There is first chain stretching along the molecular axis starting at ca. 85 °C with the emergence of the (008) reflection, implying that PFO stems within the nuclei become fully extended only near the end of the nucleation stage. This is followed by improved transverse packing along the crystallographic *b* axis with the emergence of the (200) reflection near 90 °C and eventually fully developed 3-D positional order with the emergence of (110) and other (*hk*0) peaks above 100 °C. The sequence of ordering here is consistent with earlier observations of preferred growth along the crystallographic *b* axis and faceting along the (100) and (110) planes in melt crystallization. This limited ordering along the crystallographic *c* axis developed only late in the nucleation stage implies that the molecular axis is most likely lying *transverse* to the long axis of the prolate ellipsoid, such that only limited extension of PFO chains is needed for nucleation. More evidence in support of this picture will be presented later in the text.

Growth. In the temperature range of 95−105 °C (Figure 5), an interference peak emerged in the SAXS profile and remained at the same position of $q_c = 0.0272$ Å^{-1}. This indicates fixed mean center-to-center spacing (which differs from the long period L of stacked crystalline lamellae), $d \approx 29.0$ nm (as estimated from $d = 7.884/q_c$ for *distorted* FCC packing of ellipsoids),[17] between neighboring nuclei and an essentially saturated concentration of nuclei, $n_p \approx d^{-3}$, above 90 °C. Furthermore, the scattering invariant (Q_{inv}) increased strongly with a significant decrease (by ca. 40%) in the interference peak width, suggesting improved spatial arrangement (or intergrain correlation) of nanograins in this narrow temperature range; the accompanied growth of nanograins is better illustrated by the $P(q)$ and $S(q)$ curves extracted below. Note also that nanograins with $R_g \approx 5$ nm started to give weak reflections in the corresponding WAXS profile at 105 °C, indicating concomitantly improved long-range 3-D crystalline order *within* the growing nanograins.

To extract morphological characteristics of concentrated PFO nanograins from SAXS profiles with a prominent interference peak (Figure 5), the form factor $P(q)$ and the structure factor $S(q)$ have to be resolved simultaneously. As the sharp interference peak resembles that observed in colloids of significant interparticle interactions or distorted FCC packing,[23] we have adopted a simplified hard-sphere $S(q)$ with an effective diameter.[24,25] Demonstrated in Figure 5 are the SAXS profiles adequately fitted using the hard-sphere $S(q)$ and $P(q)$ of ellipsoids,[24,25] with the semimajor and semiminor axes (A, B) ≈ (8.8 nm, 2.8 nm) and (10.0 nm, 3.3 nm). The corresponding R_g values are 4.3 and 5.0 nm at 95 and 105 °C, respectively. Note that the *shape anisotropy* of the nanograins is retained from the nucleation stage to the growth stage, with the aspect ratio A/B increasing slightly from ca. 2.7 to 3.1. In combination with the improved order along both the crystallographic *c* axis and more extensively along the *b* axis as indicated by the corresponding WAXS profiles in Figure 4, it is likely that the prolate long axis A coincides with the crystallographic *b* axis, with the chain axis lying transversely. This is consistent with the suggested molecular arrangement for nuclei.

Coalescence. From 115 to 145 °C, SAXS profiles (Figure 6a) displayed a continuous shift of the interference peak from $q_c = 0.0253$ Å^{-1} to $q_c = 0.0169$ Å^{-1} with a minor decrease (by ca. 30%) in peak width (from 0.0078 to 0.006 Å^{-1}). Meanwhile, the peak intensity increases largely with temperature by more than 4-fold, which can be attributed mainly to a size growth effect (I_o grows from 0.58 to 1,1, 1.7, and 2.5 cm^{-1}) on the basis of the fitted $P(q)$ and $S(q)$ profiles extracted (inset of Figure 6a); consistent with this attribution, corresponding WAXS profiles (Figures 4 and 6b) demonstrate concomitantly developed reflections. Using the same ellipsoidal form factor and hard-sphere structure factor, we fitted respectively the SAXS profiles at 115, 125, 135, and 145 °C (Figure 6a) to yield ellipsoid dimensions (A, B) of (2.5 nm, 8.3 nm), (3.1 nm, 10.1 nm), (4.1 nm, 12.0 nm), and (5.0 nm, 13.7 nm), with corresponding R_g values of 5.4, 6.5, 7.8, and 9.2 nm. To reconcile simultaneous increases in both the nanograin size and the center-to-center intergrain distance, we propose the coalescence of prolate ellipsoids into oblate ellipsoids for the development of lamellar crystals. This coalescence process is possible only in the direction transverse to the chain axis, which in turn supports the notion that molecular stems are oriented transversely to the major axis of the prolate nuclei. Also suggested is the concomitant thickening of the crystalline lamellae, resulting in slight increases in the aspect ratio A/B from 0.30 to 0.36.

Shortly (ca. 1 min) after reaching 145 °C for isothermal annealing, there are few further changes in both SAXS and WAXS profiles (Figure 6c), indicating quick completion of the coalescence-thickening process at a given temperature; this is characteristically different from the classical (and much slower) case of lamellar thickening during long-term isothermal annealing at an elevated temperature. In the previously proposed mechanism,[8] attachment and coalescence of nanocrystals requires nanograin alignment via thermally activated fluctuations of neighboring nanocrystals. As coalescence proceeds, the size of the nanocrystals quickly reaches a critical value at which nanograin alignment for attachment via thermal fluctuations becomes inhibited. In other words, the final morphology corresponds to coalesced nanocrystals whose size is determined by the final temperature of the cold crystallization process.

Thermal Events. During the entire heating process to induce cold crystallization, the DSC trace (Figure 6d) exhibits a clear exotherm in the range of 70−110 °C, reflecting the formation of nanograins in the nucleation stage up to $T_2 \approx 90$ °C and (with a change in slope at 95 °C) in the subsequent growth stage up to $T_3 \approx 110$ °C. In other words, although little long-range positional order is developed, the nucleation process releases a majority of the crystallization enthalpy; there are also minor contributions from the subsequent growth process. For the coalescence stage above 110 °C, no discernible thermal events can be identified at all; this stage is therefore characterized by an increase in crystal size without any significant increase in the total volume of crystallites.

Summary. Figure 7 summarizes the structural information revealed by in situ SAXS/WAXS/DSC for the cold crystalliza-

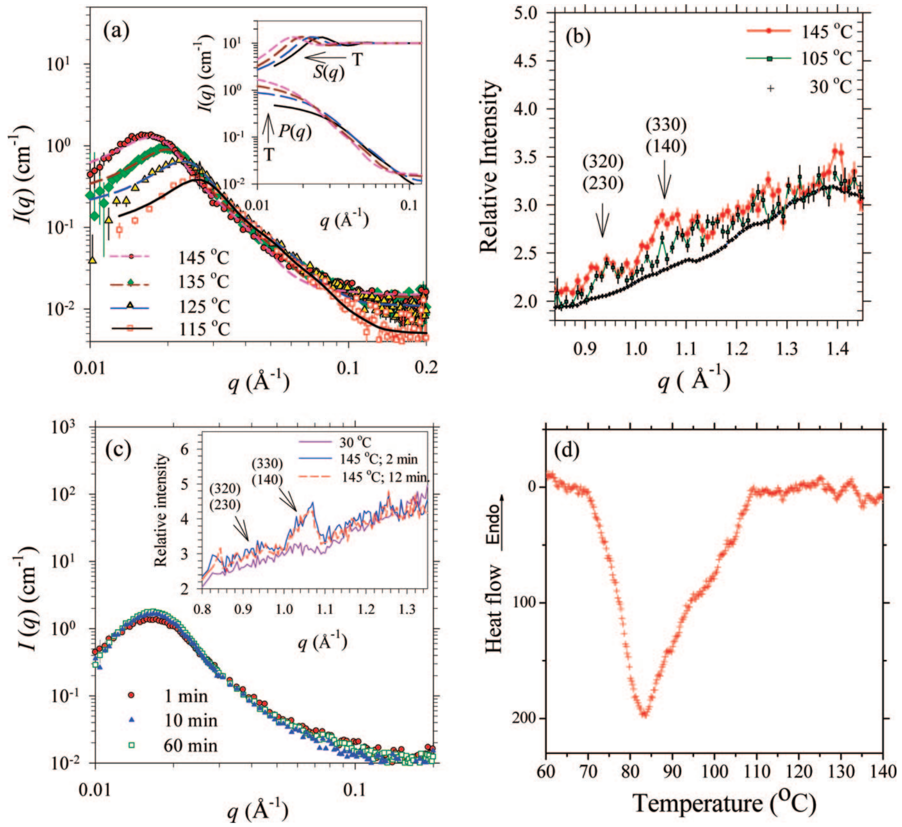

Figure 6. (a) SAXS profiles obtained at 115−145 °C, model-fitted with a combination of ellipsoid form factor $P(q)$ and hard-sphere structure factor $S(q)$. The inset shows the corresponding $P(q)$ (I_o multiplied) and $S(q)$ profiles extracted from the model fitting, with $S(q)$ profiles scaled up by a factor of 10 for clarity; arrows indicate the directions of increasing temperature. (b) Corresponding WAXS profiles. (c) In situ SAXS profiles obtained during isothermal annealing at 145 °C, with WAXS profiles given as an inset. (d) DSC trace obtained during heating (10 °C /min) from 30 to 145 °C.

tion process of PFO. The frozen-in stage before T_1 ($\sim T_g$) is eventless and hence trivial. In the nucleation stage between T_1 and T_2 ($\sim$90 °C), anisotropic nuclei of similar size and shape emerge and increase in number. Concurrently, the fast growth of the scattering invariant Q_{inv} reflects the significantly increased degree of heterogeneity due to the formation of nanograins (Figure 7b). In the growth stage between T_2 and T_3 ($\sim$110 °C), nanograins (of fixed concentration n_p) grow anisotropically as prolate ellipsoids (cf. the A/B ratio and R_g curves in Figure 7a) and develop into a micellelike distorted-FCC arrangement, resulting in extensively developed heterogeneity and, thus, rapidly increased Q_{inv}. Thermal events concerning cold crystallization are essentially completed at the end of this stage as revealed by DSC (Figure 6d), although the WAXS results (Figures 3b and 4) indicate little long-range positional order.

In the coalescence stage above T_3, the nanograins grow by coalescence, resulting in a rapid increase in size with an accompanied shape transformation from prolate to oblate ellipsoids (cf. the A/B ratio in Figure 7a). Such shape transformation is consistent with attachment and coalescence of nanograins transverse to the chain axis (giving clear ($hk0$) reflections in the WAXS profiles; cf. Figures 4 and 6b) to result in an extensively developed lateral dimension (up to 27 nm in terms of the minor axis), with some concomitant ordering and hence lamellar thickening along the chain axis (up to ca. 10 nm in terms of the major axis), as shown schematically in Figure 7c. This coalescence process does not involve significant changes in the degree of heterogeneity, as evidenced by the nearly constant Q_{inv} (Figure 7b), nor does it involve any discernible thermal events, as the DSC trace has already returned to the baseline (Figure 6d). On the other hand, the crystallinity $X_{c,WAXS}$ extracted from the WAXS profiles (of clear ($hk0$) reflections) is developed mainly in this stage (Figure 7b), indicating a drastic increase in the long-range positional order transverse to the molecular axis that is consistent with the steadily increasing lateral size beyond 20 nm (Figure 7a).

Discussion

Nucleation. As stated earlier, the nucleation stage constitutes a majority of the exothermic activity of the cold crystallization process. This implies solidlike molecular packing within the nuclei, as evidenced by the adequate contrast for SAXS observations. Curiously, although the number of nuclei increased clearly with temperature, the nuclei formed are characterized by a *fixed* size ($R_g \approx 3.3$ nm) and shape (aspect ratio $A/B \approx 2.7$); in spite of some stem straightening for improved order along the molecular axis, growth is allowed only later in the subsequent stage at further raised temperatures. We have argued (on the basis of WAXS results in Figure 4, subsequent observations in the growth and coalescence stages, and the well-known tendency of polymers to give lamellar crystals) that these nuclei correspond to laterally aggregated stems with the molecular axis lying transverse to the long axis of the prolate ellipsoid. This is reminiscent of both the fringed-micelle model[26] for nanometer-sized crystallites and the more recent "bundle" model of Allegra et al.[27] for the nucleation of polymer crystals. As the stems aggregate, entangled chains in the immediate neighborhood are expected to become more tightly locked: only limited reptational displacement is expected in view of the low mobility of chains at temperatures less than 25 °C above T_g. This not only sets a natural limit to the nuclear size/shape but also excludes further nucleation in the "knotted" vicinity of an existing nucleus. The latter results in subsequent nucleation at sites midway between two neighboring nuclei and hence the

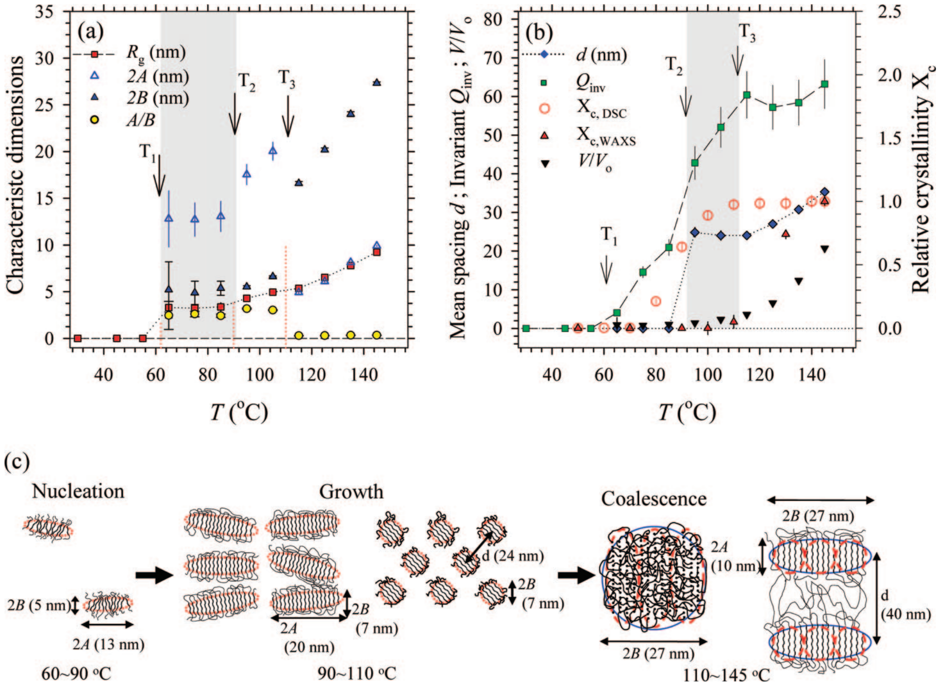

Figure 7. (a) Temperature-dependent major axis 2*A* and minor axis 2*B*, aspect ratio *A*/*B*, and R_g of ellipsoid-like PFO nanograins in the cold crystallization process. (b) Mean spacing *d* (calculated from the fitted nanograin concentration), relative scattering invariant Q_{inv} (scaled up by a factor for clarity), normalized volume V/V_o (with respect to nanograins formed near the end of the nucleation stage, i.e., 85 °C), and crystallinity extracted from the DSC trace ($X_{c,DSC}$) and that from WAXS profiles ($X_{c,WAXS}$). Onset temperatures of the nucleation, growth, and coalescence stages are respectively denoted as T_1 (~62 °C), T_2 (~90 °C), and T_3 (~110 °C). (c) Cartoons (from left to right) illustrating structural evolution of PFO nanograins from the nucleation stage (sparsely emerged prolate nuclei, side view) to the growth stage (prolate ellipsoids, side and end views transverse to the molecular axis) and the coalescence stage (oblate ellipsoids, top and side views along and transverse to the molecular axis, respectively).

distorted-FCC-like structure at the end of this nucleation stage, yielding a clearly emerged SAXS peak early in the growth stage (compare Figures 3a and 5). This signifies a sharp demarcation between the nucleation and the growth stages across T_2.

Growth and Coalescence. With a further increase in temperature after saturated nucleation into a distorted FCC lattice, increased chain mobility results in relaxed knots and hence more extensive aggregation of longer stems and growth of nuclei into nanocrystals of identifiable WAXS reflections in the growth stage. As the long dimension (i.e., the major axis $2A \approx 20$ nm) of the nanograins started to approach the spacing (ca. 24 nm) between nearest neighbors at 105 °C, further growth of nanograins resulted in spatial conflicts. This sets the stage for the competing mechanism of orientated attachment and coalescence of nanograins, which requires both close proximity of the nanograins and thermally activated rotation. As schematically demonstrated in Figure 7c, the nematic nature of the as-quenched glass ensures that subsequently developed nanograins are more-or-less oriented; this presumably facilitates the coalescence process, as only moderate amplitudes of nanograin rotation are required. In the melt crystallization of sheared specimens, anisotropic growth (i.e., a strongly retarded growth rate upon mismatched molecular orientation at crystal fronts) has been observed to result in butterfly-like spherulites.[7] As coalescence requires proximity of the nanograins, which depends on local variations of the nanograin position/size, the transition from the growth stage to the coalescence stage is unlikely to be sharp. Hence, apparent discontinuities in the switching of major and minor axes across the transition temperature T_3 (Figure 7a) are somewhat artificial and at least partly attributable to the limitations of the analytical model shapes adopted.

Comparison with Earlier Nanograin Models. Strictly speaking, the present notion of nanograins should be limited to stereo- or regioregular conjugated polymers with flexible side chains that exhibit a clear tendency toward crystallization. Nevertheless, as similar features of nanograins have been reported in the literature for typical polymers, it appears appropriate to comment on possible connections or intrinsic differences. Also well-known is the presence of nanometer-sized "blocks" in fibers of semicrystalline polymers, demonstrated by Perterlin[28] more than three decades ago. These nanocrystalline blocks were attributed to fracturing of crystalline lamellae upon extensive drawing, where defects were considered the weak points for the initiation of plastic deformation. An interesting link between the two apparently different attributions is the observation of a large number of dislocations along the plane of attachment in coalesced crystals.[9,10]

Grainy features in melt-crystallized polymers noted in recent years by Strobl et al.[12,29] have led to the proposal of mesomorphic nodules at the crystal front as precursors to crystallization. Nanograins in PFO, however, may be somewhat different in molecular origin, as nanodomains have been extensively identified for both quenched nematic PFO glass and even noncrystalline conjugated polymers of alkyl side chains. It is nevertheless tempting to relate the solidlike molecular packing, the lack of crystal-like reflections, and the stagnant size without growth of the nuclei to the "mesophase" precursor hypothesized by Strobl. On the other hand, the proposed mesomorphic clusters at the crystal front might very well be attributed to surface-induced (or stabilized) nucleation while similar nuclei formed in the bulk melt remain unstable and transient.[8] Within the present scope, it is indeed simpler (and hence tentatively preferable according to Occam's razor principle) to attribute the lack of clear WAXS reflections up to 85 °C just to the limited size of the nuclei (13 nm in length but only 5 nm in width).

Comparison with the Spinodal Model. Previous SAXS/WAXS studies of cold crystallization for a variety of polymers indicated an "induction" or "incubation" stage, where a SAXS peak increased intensity with time at a constant peak position before any detectable WAXS reflections; in the subsequent "crystallization" stage with WAXS reflections, the SAXS peak shifted to a lower q position with a continuous growth in intensity.[11,30−32] As the stationary position and increasing intensity of the SAXS peak are reminiscent of the spinodal decomposition (SD) of binary mixtures, the induction stage has been modeled as SD-like,[32] with constant phase dimensions but increasing contrast in density. Note that our *nucleation* stage for PFO bears no direct counterpart in SD, despite that *growth* and *coalescence* correspond to the incubation and the crystallization stages, respectively. In addition, in a minority report, Wang et al.[33] also favored an interpretation with nucleation-and-growth rather than SD, based on an observed high-q shift, rather than the low-q shift, of the SAXS interference peak in isothermal cold crystallization of polyethylene.

Most of the earlier SAXS/WAXS reports on cold crystallization drew only qualitative or kinetic analogy toward spinodal decomposition, but Ryan et al.[11] indeed devised an interesting theoretical frame. On first look, two key pillars in the classical SD theory[34] are clearly missing in crystallization as opposed to liquid−liquid phase separation: the conservation of population for the two components in the separating phases and the negative curvature (i.e., a hump) of free energy at intermediate compositions of the phase diagram. For the former, analogy was drawn by taking the specific (say, *trans*) conformation in the crystalline state as one component and all other conformations collectively as the second component, i.e., considering each chain as a "conformational copolymer". To give a region of negative curvature in the central portion of the free energy curve, a quadratic density−conformation coupling term was introduced to the Landau expression for a BCC-like Fourier mode. These in combination result in a picture of two modulated "phases" which are rich and poor in the preferred conformation.

It should be pointed out that, within this framework, population conservation is not intrinsic: the *trans* conformation will eventually be the dominating conformer via annihilation of sequentially connected unfavorable conformers (e.g., $g^+ + g^- \rightarrow 2t$) and relaxation through chain ends. However, as reptation is slow at temperatures only mildly above T_g, chain contour is confined and conformer dynamics limited in the early stage of cold crystallization; conservation of conformer populations may hence be *approximated* in this combined temperature/time limit. Note that these conditions are similar to our arguments for fixed nuclear size and increasing nuclear density during the nucleation stage of PFO cold crystallization. In addition, the use of a BCC-like Fourier mode in Ryan's SD theory coincides with the present case of nuclei in a distorted FCC arrangement in real space (rather than the traditional 1-D model of striated domains) as reflected in their schematic illustration (Figure 12 therein).[11] It hence appears that the nucleation-and-growth and Ryan's SD models are essentially equivalent in describing the early stage of cold crystallization. However, the present picture of nucleation, growth, and coalescence is clearly more specific.

Concluding Remarks

Earlier SAXS/WAXS studies[30−33,35,36] of density fluctuations prior to polymer crystallization typically adopted the correlation function or scattering invariant, which gave only indirect information on morphological features before the formation of crystalline lamellae. On the basis of our previous microscopic results, we have modeled nanograins with the analytical shape of ellipsoids and interpreted the observed density fluctuations during cold crystallization of PFO in terms of nucleation, growth, and coalescence of nanograins. The final morphology is therefore coalesced nanocrystallites, which are kinetically trapped as the size reaches a critical value such that nanograin alignment for attachment−growth via thermal fluctuations is seriously hindered at the final temperature. Relevance to earlier concepts of nanocrystalline blocks, mesomorphic precursors, and the SD mechanism in the early stage of cold crystallization are addressed. For more direct comparison, it would be interesting to investigate the cold crystallization of a more typical polymer of random-coil chains; one such study on syndiotactic polystyrene is in progress, and the results are to be reported shortly.

Acknowledgment. Financial support from the National Science Council (Grant Numbers NSC96-2221-E-007-015 and NSC96-2112-M-213-008-MY3) is gratefully acknowledged.

References and Notes

(1) Chen, S. H.; Su, A. C.; Chou, H. L.; Peng, K. Y.; Chen, S. A. *Macromolecules* **2004**, *37*, 167.
(2) Chen, S. H.; Su, A. C.; Han, S. R.; Chen, S. A.; Lee, Y. Z. *Macromolecules* **2004**, *37*, 181.
(3) Chen, S. H.; Su, C. H.; Su, A. C.; Chen, S. A. *J. Phys. Chem. B* **2004**, *108*, 8855.
(4) Jeng, U.; Hsu, C. H.; Sheu, H. S.; Lee, H. Y.; Inigo, A. R.; Chiu, H. C.; Fann, W. S.; Chen, S. H.; Su, A. C.; Lin, T. L.; Peng, K. Y.; Chen, S. A. *Macromolecules* **2005**, *38*, 6566.
(5) Chen, S. H.; Chou, H. L.; Su, A. C.; Chen, S. A. *Macromolecules* **2004**, *37*, 6833.
(6) Chen, S. H.; Su, A. C.; Chen, S. A. *J. Phys. Chem. B* **2005**, *109*, 10067.
(7) Chen, S. H.; Su, A. C.; Chen, S. A. *Macromolecules* **2006**, *39*, 9143.
(8) Chen, S. H.; Wu, Y. H.; Su, C. H.; Jeng, U.; Hsieh, C. C.; Su, A. C.; Chen, S. A. *Macromolecules* **2007**, *40*, 5353.
(9) Penn, R. L. *J. Phys. Chem. B* **2004**, *108*, 12707, and references therein.
(10) Shen, P.; Fahn, Y. Y.; Su, A. C. *Nano Lett.* **2001**, *1*, 299, and references therein.
(11) Ryan, A. J.; Fairclough, J. P. A.; Terrill, N. J.; Olmsted, P. D.; Poon, W. C. K. *Faraday Discuss.* **1999**, *112*, 13, and references therein.
(12) Strobl, G. *Eur. Phys. J. E* **2000**, *3*, 165, and references therein.
(13) Lai, Y. H.; Sun, Y. S.; Jeng, U.; Lin, J. M.; Lin, T. L.; Sheu, H. S.; Chuang, W. T.; Huang, Y. S.; Hsu, C. H.; Lee, M. T.; Lee, H. Y.; Liang, K. S.; Gabriel, A.; Koch, M. H. J. *J. Appl. Crystallogr.* **2006**, *39*, 871.
(14) Chen, S. H.; Su, C. H.; Su, A. C.; Sun, Y. S.; Jeng, U.; Chen, S. A. *J. Appl. Crystallogr.* **2007**, *40*, s573.
(15) Bark, M.; Zachmann, H. G. *Acta Polym.* **1993**, *44*, 259.
(16) Chu, B.; Hsiao, B. S. *Chem. Rev.* **2001**, *101*, 1727.
(17) Chen, S. H.; Lin, T. L. In *Methods of Experimental Physics—Neutron Scattering in Condensed Matter Research*; Sköld, K., Price, D. L., Eds.; Academic: New York, 1987; Vol. *23B*, Chapter 16.
(18) Feigin, L. A.; Svergun, D. I. *Structure Analysis by Small-Angle X-ray and Neutron Scattering*; Plenum: New York, 1987; p 69.
(19) Terrill, N. J.; Fairclough, P. A.; Towns-Andrews, E.; Komanschek, B. U.; Young, R. J.; Ryan, A. J. *Polymer* **1998**, *39*, 2381.
(20) Wang, Z.-G.; Hsiao, B. S.; Sirota, E. B.; Srinivas, S. *Polymer* **2000**, *41*, 8852.
(21) Chuang, W.-T.; Jeng, U.; Sheu, H.-S.; Hong, P.-D. *Macromol. Res.* **2006**, *14*, 45.
(22) Teixeira, J. *J. Appl. Crystallogr.* **1988**, *21*, 781.
(23) Chen, S. H.; Sheu, E. Y.; Kalus, J.; Hoffmann, H. *J. Appl. Crystallogr.* **1988**, *21*, 751, and references therein.
(24) Krakovasky, I.; Urakawa, H.; Kajiwara, K. *Polymer* **1997**, *14*, 3645.
(25) Huang, Y.-Y.; Hsu, J.-Y.; Chen, H.-L.; Hashimoto, T. *Macromolecules* **2007**, *40*, 406.
(26) Geil, P. H. *Polymer Single Crystals*; Wiley: New York, 1973; pp 7−10.
(27) Allegra, G.; Meille, S. V. *Adv. Polym. Sci.* **2005**, *191*, 87, and references therein.
(28) Peterlin, A. *Text. Res. J.* **1972**, *42*, 20.
(29) Strobl, G. *Prog. Polym. Sci.* **2006**, *31*, 398, and references therein.
(30) Kaji, K.; Nishida, K.; Kanaya, T.; Matsuba, G.; Konishi, T.; Imai, M. *Adv. Polym. Sci.* **2005**, *191*, 187, and references therein.
(31) Schultz, J. M.; Lin, J. S.; Hendricks, R. W.; Petermann, J.; Gohil, R. M. *J. Polym. Sci., Part B: Polym. Phys.* **1981**, *19*, 609.
(32) Heeley, E. L.; Poh, C. K.; Li, W.; Maidens, A.; Bras, W.; Dolbnya, I. P.; Gleeson, A. J.; Terrill, N. J.; Fairclough, J. P. A.; Olmsted, P. D.; Ristic, R. I.; Hounslow, M. J.; Ryan, A. J. *Faraday Discuss.* **2002**, *122*, 343.
(33) Wang, Z.-G.; Hsiao, B. S.; Sirota, E. B.; Srinivas, S. *Polymer* **2000**, *41*, 8825.
(34) Cahn, J. W.; Hilliard, J. E. *J. Chem. Phys.* **1958**, *28*, 25.
(35) Fougnies, C.; Damman, P.; Villers, D.; Dosiere, M.; Koch, M. H. J. *Macromolecules* **1997**, *30*, 1385–1391.
(36) Mano, J. F.; Wang, Y.; Viana, J. C.; Denchev, Z.; Oliveira, M. J. *Macromol. Mater. Eng.* **2004**, *289*, 910.

MA801177H